Journal of Fluids and Structures 87 (2019) 284–301

Contents lists available at ScienceDirect

Journal of Fluids and Structures

journal homepage: www.elsevier.com/locate/jfs

Response of a linear viscoelastic splitter plate attached to a cylinder in laminar flow

Rahul Mishra [a], Salil S. Kulkarni [b], Rajneesh Bhardwaj [b,*], Mark C. Thompson [c]

[a] IITB-Monash Research Academy, IIT Bombay, Mumbai, 400076, India
[b] Department of Mechanical Engineering, IIT Bombay, Mumbai, 400076, India
[c] Fluids Laboratory for Aeronautical and Industrial Research (FLAIR), Department of Mechanical and Aerospace Engineering, Monash University, Clayton 3800, Australia

ARTICLE INFO

Article history:
Received 1 October 2018
Received in revised form 5 February 2019
Accepted 27 March 2019
Available online 17 April 2019

Keywords:
Fluid–structure interaction
Viscoelastic splitter plate
Standard linear solid
Immersed boundary method

ABSTRACT

The flow-induced deformation of a viscoelastic thin plate attached to the lee side of a circular cylinder subjected to laminar flow is numerically investigated. An in-house fluid–structure interaction solver couples the sharp-interface immersed boundary method for fluid dynamics with a finite-element method for structural dynamics. Extending published results on elastic materials, the *Standard Linear Solid* (SLS) model is used to represent viscoelasticity of the plate, governed by the following two parameters: (a) the ratio of the non-equilibrium to equilibrium Young's modulus (R), and (b) the ratio of dimensionless material damping to the dimensionless non-equilibrium Young's modulus (τ). The focus of the present study is to examine the dynamic response of the viscoelastic plate at Reynolds number of $Re = 100$. The amplitude and the time to achieve a dynamic steady state of a plate with $0.1 < R < 5$ and $0.1 < \tau < 10$ have been investigated. The plate attains a self-sustained time-periodic oscillation with a plateau amplitude for the range of R =[0.1–5] for all values of τ. The dimensionless tip displacement amplitude ($A_{Y,tip}$) is found to be a non-monotonic function of τ. When the forcing frequency (vortex shedding frequency) is lesser (greater) than the natural frequency (considering the equilibrium Young modulus) of the plate, $A_{Y,tip}$ decreases (increases) asymptotically. The theoretical analysis of a simple spring–mass–dashpot model of SLS is undertaken to understand the effect of sinusoidal forcing on the plate dynamics. Analytical predictions show general agreement with the non-monotonic behaviour of the numerically computed $A_{Y,tip}$. The results suggest that careful tuning of the damping may be effectively employed to enhance power output for energy extraction applications or to suppress flow-induced vibration when it is detrimental to the structure.

1. Introduction

The flow-induced deformation of flow around a flexible structure from fluid forcing can in turn alter the flow field, resulting in a coupled process called Fluid–Structure Interaction (FSI), and a subset known as Flow-Induced Vibration (FIV), have various applications in engineering and biology. Examples of FSI in biological systems occur in the cardiovascular

* Corresponding author.
E-mail address: rajneesh.bhardwaj@iitb.ac.in (R. Bhardwaj).

https://doi.org/10.1016/j.jfluidstructs.2019.03.026
0889-9746/

system (Mittal et al., 2016) and vocal folds (Mittal et al., 2011). In such systems, structural flexibility augmented with flow-induced vibration is a key feature in biological locomotion, including fish swimming and bird flight (Mittal, 2004).

The computational modelling of the large-scale flow-induced deformation of a thin structure is challenging and it involves accurate tracking of the deforming structure boundary immersed in the fluid domain. The Immersed boundary (IB) method is well-suited for problems in fluid–structure interaction including those involving large deformation (Bhardwaj and Sharma, 2017). As discussed by Mittal and Iaccarino (2005), the IB method allows accurate tracking of the deforming, three-dimensional, complex, moving boundaries on a Cartesian grid. Since the governing equations are solved on a body non-conformal Cartesian grid, there is no need for remeshing to treat deforming or moving structure boundaries in the fluid domain, provided spatial resolution is adequate in the fluid domain. IB methods can be classified in two categories (Mittal and Iaccarino, 2005), namely, the continuous-forcing or diffuse-interface approach, and the discrete-forcing or sharp-interface approach. In the former, a source term is added in the momentum equation to represent the immersed structure boundary. The "diffuse" boundary implies that the boundary condition is satisfied within a local region (a few cells) near the boundary. While in the latter, the governing equations are first discretized on the Cartesian grid without treating the structure boundary and subsequently discretization in the cells near the boundary is modified. This approach yields a "sharp" representation of the boundary. i.e. the boundary condition on the immersed boundary is exactly satisfied to the order of the discretization. The continuous forcing approach was first proposed by Peskin (1972) and since then many variants of the diffuse IB method have been reported. For example, Miao et al. (2017) developed a fully coupled immersed flow solver for a three-dimensional simulation of fluid–fluid interaction. Similarly, several studies reported the development of the sharp-interface method (Fadlun et al., 2000; Udaykumar et al., 2001; Mittal et al., 2008; Seo and Mittal, 2011; Bailoor et al., 2017).

The physics governing the interaction of an elastic, inextensible plate/filament attached to a cylinder under laminar fluid flow has been reported in previous studies. A FSI benchmark for the flow past an elastic splitter plate attached to the lee side of a rigid cylinder in two-dimensional laminar channel flow was proposed by Turek and Hron (2006). They showed that the flow-induced deformation of the plate results in a self-sustained oscillation of the plate. Extensive studies have been carried out on the interaction between flexible splitter plates and a moving fluid, theoretically (Eloy et al., 2007), numerically (Connell and Yue, 2007) and experimentally (Shelley et al., 2005). Bhardwaj and Mittal (2012) quantified the effect of Reynolds number, material properties and geometric non-linearity on the plate displacement. Shukla et al. (2013) experimentally studied the effects of flexural rigidity and plate length on the response of a plate in the wake of a circular cylinder. They found that the plate displacement collapses onto a single curve for different cases of dimensionless bending stiffness ($E^*h^{*3}/12\rho_f^*U^{*2}L^{*3}$) for a given splitter plate length. Furquan and Mittal (2015) investigated flow past two side-by-side square cylinders with flexible splitter plates and observed that the lock-in occurs at a plate frequency close to its first natural frequency. The lock-in can be described as a synchronization of the vortex shedding frequency of the coupled system (Strouhal number) with the natural frequency of the flexible structure. Flow past a cylinder with a flexible splitter plate of a Saint Venant–Kirchhoff type material has been studied by Lee and You (2013). The drag and lift coefficient, and tip displacement, of the flexible plate is a monotonic function of bending stiffness, for a plate length of $l = 3D$, whereas it is a non-monotonic function of bending stiffness for $l = 1D$ and $2D$. The amplitude of the displacement of the structure is large if the vortex shedding frequency is close to the dominant natural frequency of the splitter plate.

Most of the previous studies have considered only elastic flexible thin structures, while very few studies have reported the response of viscoelastic structures. Structural damping reduces acoustic and dynamic response due to the energy dissipating property of the materials. In the context of modelling of viscoelasticity of only structure (i.e without fluid), De Haan and Sluimers (2001) reported dynamic behaviour of a standard linear solid viscoelastic material. There has been significant work done on the fluid–structure interaction in conduits with viscoelastic walls, such as fluid flow inside a pipe (Keramat et al., 2012) and blood flows in arteries (Wang et al., 2015). Keramat et al. (2012) studied water hammer in a pipeline that has a viscoelastic wall, modelled by Kelvin–Voigt model. Wang et al. (2015) studied viscoelasticity of the walls of the carotid artery subjected to pulsatile flow. Fewer works have been undertaken on the flutter of a viscoelastic plate. Of these, studies by Ilyasov and Ilyasova (2006), Matyash (1971), and Kiiko (1996) have studied the stability of a viscoelastic plate. They used the Kelvin–Voigt fractional-order constitutive relation for modelling the viscoelasticity. Chen et al. (2014) studied the effects of material viscoelasticity on the dynamics of a flag in a flow. Scott–Blair model (Rogosin and Mainardi, 2014) and Kelvin–Voigt model have been used to represent the viscoelasticity of the flag material.

As discussed above, previous studies used the Kelvin–Voigt (KV) model, which can describe the creep behaviour but it cannot describe the stress relaxation. Therefore, in the present study, the *standard linear solid model (SLS)* (Huang and Huang, 1971; Esmailzadeh and Jalali, 1999) is used to study the effect of material viscoelasticity. The SLS model is the simplest linear viscoelastic model, which describes an intermediate mechanical state between an elastic structure and a fluid, that predicts both creep or recovery and stress relaxation (Findley and Davis, 2013). We implement the SLS model in an in-house FSI solver, which couples a sharp-interface immersed boundary method for the fluid dynamics with a finite-element method for the structural dynamics. The vibration response of a viscoelastic structure immersed in a fluid governed by the SLS has not been investigated thus far, to the best of our knowledge. In order to understand the interaction of a viscoelastic structure with the fluid flow, we extend the FSI benchmark case of Turek and Hron (2006) for an elastic plate to a linear viscoelastic plate. In this benchmark, a thin plate attached to the lee side of a cylinder in mounted in a channel flow. The plate is free to oscillate and attains a self-sustained time-periodic oscillation with a plateau amplitude. Here, we show that the non-linear interaction of the steady flow with the moving viscoelastic structure leads to a non-monotonic behaviour of amplitude with material damping.

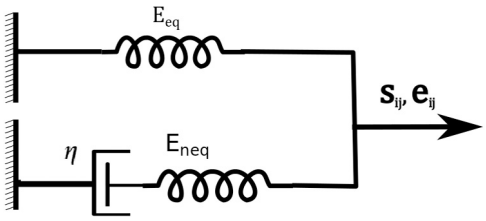

Fig. 1. Schematic of the SLS model used for viscoelastic structure.

The layout of this paper is as follows. In Section 2, the governing equations for the structure (viscoelastic plate), fluid flow, and coupling of the flow and structural solvers are provided. The numerical approach to solve this coupled system is also briefly discussed. In Section 3, an analytical solution of a simple mass–spring–dashpot (MSD) model of SLS is presented. In Section 3.2, the MSD model is solved analytically, which helps to predict the complex phenomenon of FSI with SLS model. The simulation results are given in Section 4, as function of two parameters in the SLS model. These parameters are: (a) the ratio of the non-equilibrium to equilibrium Young's modulus (R), and (b) the ratio of dimensionless material damping to the dimensionless non-equilibrium Young's modulus (τ). The influence of these parameters on the amplitude of the plate and time to achieve self-sustained oscillation are quantified.

2. Computational model

We extend an in-house FSI solver (Bhardwaj and Mittal, 2012) in the present work to account for viscoelasticity of the structure. The FSI solver is built upon previous works of Mittal and co-workers (Mittal et al., 2008; Seo and Mittal, 2011) and combines a sharp-interface immersed boundary method flow model with a finite-element based structure dynamics solver. The governing equations of the flow domain are solved on a fixed Cartesian (Eulerian) grid while the movement of the immersed structure surface is tracked through a Lagrangian framework. The flow is governed by the time-dependent viscous and incompressible Navier–Stokes equations:

$$\frac{\partial v_i}{\partial x_i} = 0, \tag{1}$$

$$\frac{\partial v_i}{\partial t} + \frac{\partial v_j v_i}{\partial x_j} = -\frac{\partial p}{\partial x_i} + \frac{1}{Re}\frac{\partial^2 v_i}{\partial x_j^2}, \tag{2}$$

where $i, j = 1, 2$, and v_i, t, p and Re represent the velocity components, time, pressure and the Reynolds number. Some important variables used in the model are defined in Table 1. These equations are discretized in space using a cell-centred, collocated (non-staggered) arrangement of the primitive variables (v_i, p) using a second-order, central-difference scheme for all spatial derivatives. The detailed computational methodology can be found in previous papers (Mittal et al., 2008; Seo and Mittal, 2011; Bhardwaj and Mittal, 2012; Kundu et al., 2017).

The structure dynamics was simulated using an open-source finite-element-based structural dynamics solver, Tahoe© (Tahoe, 2001). The constitutive model of the structure is considered as Standard Linear Solid (SLS). Fig. 1 shows the schematic of SLS model and it incorporates the viscoelastic Young's moduli, E_{neq}, E_{eq}, and the viscoelastic dissipation, η.

For an isotropic homogeneous linear viscoelastic material, the constitutive relation between the stress and strain is given by Christensen (2012) and Huang and Huang (1971):

$$\begin{aligned} P_1 s_{ij}(t) &= Q_1 e_{ij}(t), \\ P_2 \sigma_{ii}(t) &= Q_2 \epsilon_{ii}(t), \end{aligned} \tag{3}$$

where s_{ij} and e_{ij} are the deviatoric stress and strain, respectively. σ_{ii} and ϵ_{ii} are the dilational stress and strain, respectively. For SLS model, P_1, Q_1, P_2, Q_2 are differential operators and are given by,

$$P_1 = P_2 = \left(1 + \frac{\eta}{E_{neq}}\frac{\partial}{\partial t}\right), \tag{4}$$

$$Q_1 = 2G\left(1 + \frac{E_{eq} + E_{neq}}{E_{eq}}\frac{\eta}{E_{neq}}\frac{\partial}{\partial t}\right), \tag{5}$$

$$Q_2 = 2K\left(1 + \frac{E_{eq} + E_{neq}}{E_{eq}}\frac{\eta}{E_{neq}}\frac{\partial}{\partial t}\right). \tag{6}$$

where G and K are viscoelastic shear modulus and bulk modulus, respectively.

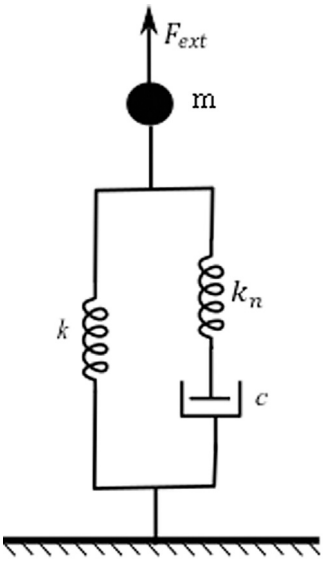

Fig. 2. Schematic of spring dash-pot model mimicking 1D Standard Linear Solid (SLS) model.

The structural solver (Tahoe, 2001) was implicitly (two-way) coupled with the in-house flow solver using an implicit partitioned approach by Bhardwaj and Mittal (2012). The implicit coupling ensures numerical stability at low structure–fluid density ratio. No slip boundary conditions are applied for the velocity at the fluid–structure interface, which represents the continuity of the velocity at the interface,

$$v_{i,f} = \dot{d}_{i,s}, \tag{7}$$

where subscripts f and s represent the fluid and structure, respectively, and d is the surface displacement. At the interface, a balance of stresses is applied,

$$\sigma_{ij,f} n_j = \sigma_{ij,s} n_j, \tag{8}$$

where n_j is the local surface normal pointing outward from the surface.

Using the FSI solver, extensive validations of benchmark problems such as flow past bluff bodies and large-scale flow-induced deformation have been reported in previous papers (Mittal et al., 2008; Seo and Mittal, 2011; Bhardwaj and Mittal, 2012; Kundu et al., 2017). Additional validations have been performed for the structural solver considering the SLS model of the viscoelastic plate in Appendix A.

3. Analysis of the SLS model

In order to describe the behaviour of a linear viscoelastic structure, a spring–dashpot model is utilized to understand the SLS model by Findley and Davis (2013). The spring describes the elastic properties and the dashpot describes the viscous properties of the structure. To understand the FSI of the viscoelastic plate, a simple mass–spring–dashpot model (MSD) (Fig. 2) with free vibration and sinusoidal applied forcing has been solved analytically. The constitutive equation of the SLS material is given by

$$F_{int} + \frac{c}{k_n}\frac{dF_{int}}{dt} = ku + c\left(1 + \frac{k}{k_n}\right)\frac{du}{dt}, \tag{9}$$

where F_{int}, u, and c are the internal force, displacement and the coefficient of damping, respectively. Here k and k_n are the spring constants parallel to c and in series with c, respectively. On combining the constitutive equation with the following dynamic equation

$$m\frac{d^2u}{dt^2} = F_{ext} - F_{int}. \tag{10}$$

the differential equation of the SLS-type rheological system is obtained as follows:

$$\frac{mc}{k_n}\frac{d^3u}{dt^3} + m\frac{d^2u}{dt^2} + c\left(1 + \frac{k}{k_n}\right)\frac{du}{dt} + ku = F_{ext} + \frac{c}{k_n}\frac{F_{ext}}{dt}. \tag{11}$$

3.1. Free vibration

The differential equation for free vibration ($F_{ext} = 0$) is given by

$$\frac{mc}{k_n}\frac{d^3u}{dt^3} + m\frac{d^2u}{dt^2} + c\left(1 + \frac{k}{k_n}\right)\frac{du}{dt} + ku = 0. \tag{12}$$

Defining the parameters for the SLS system as

$$\tau = \frac{c}{k_n}, \quad R = \frac{k_n}{k}, \quad \omega = \sqrt{\frac{k}{m}}, \tag{13}$$

Eq. (12) becomes

$$\tau\frac{d^3u}{dt^3} + \frac{d^2u}{dt^2} + \tau\omega^2(1+R)\frac{du}{dt} + \omega^2 u = 0. \tag{14}$$

Eq. (14) is third-order differential equation with constant coefficients, hence its characteristic equation is a third-degree polynomial of the form:

$$\tau r^3 + r^2 + \tau\omega^2(1+R)r + \omega^2 = 0. \tag{15}$$

To solve Eq. (15), the discriminant is given by

$$\Delta = \tau^2\omega^4\left(-27 + 18(1+R) + (1+R)^2\right) - 4\tau^4\omega^6(1+R)^3 - 4\omega^2. \tag{16}$$

If $\Delta > 0$, Eq. (15) has three negative real roots (for details see Appendix D). The solution for this case is given by

$$u = c_1e^{-z_1t} + c_2e^{-z_2t} + c_3e^{-z_3t}, \tag{17}$$

where the coefficients c_1, c_2, c_3 are depend on initial conditions. The solution decays exponentially. If $\Delta < 0$, equation Eq. (15) has one real root $r_1 = -\gamma$ and two complex conjugate roots $r_2 = -\beta - i\alpha$ and $r_3 = -\beta + i\alpha$ is given by

$$\gamma = \frac{1}{3\tau}\left(1 + C + \frac{\Delta_0}{C}\right), \tag{18}$$

$$\beta = \frac{1}{3\tau} - \frac{C}{6\tau} - \frac{\Delta_0}{6\tau C} \tag{19}$$

and

$$\alpha = \frac{\sqrt{3}C}{6\tau} - \frac{\sqrt{3}\Delta_0}{6C\tau}, \tag{20}$$

where

$$C = \sqrt[3]{\frac{\Delta_1 + \sqrt{-27\tau^2\Delta}}{2}}, \tag{21}$$

$$\Delta_1 = 27\tau^2\omega^2 - 9\tau^2\omega^2(1+R) + 2 \tag{22}$$

and

$$\Delta_0 = -3\tau^2\omega^2(1+R) + 1. \tag{23}$$

The solution of Eq. (14) for this case is given by

$$u = \underbrace{c_1e^{-\gamma t}}_{\text{Term 1}} + \underbrace{e^{-\beta t}(c_2 sin(\alpha t) + c_3 cos(\alpha t))}_{\text{Term 2}}. \tag{24}$$

The constants c_1, c_2, c_3 are determined by the initial conditions. Eq. (24)) represents two solution :

Damping Type 2 (DT1) $\gamma > \beta$, Pure exponential term (Term 1) decays out more rapidly than damped periodic term (Term 2). An example is shown in Fig. 3(a).

Damping Type 1 (DT2) $\gamma < \beta$, Damped periodic term (Term 2) decays out more rapidly than the pure exponential term (Term 1). An example is shown in Fig. 3(b).

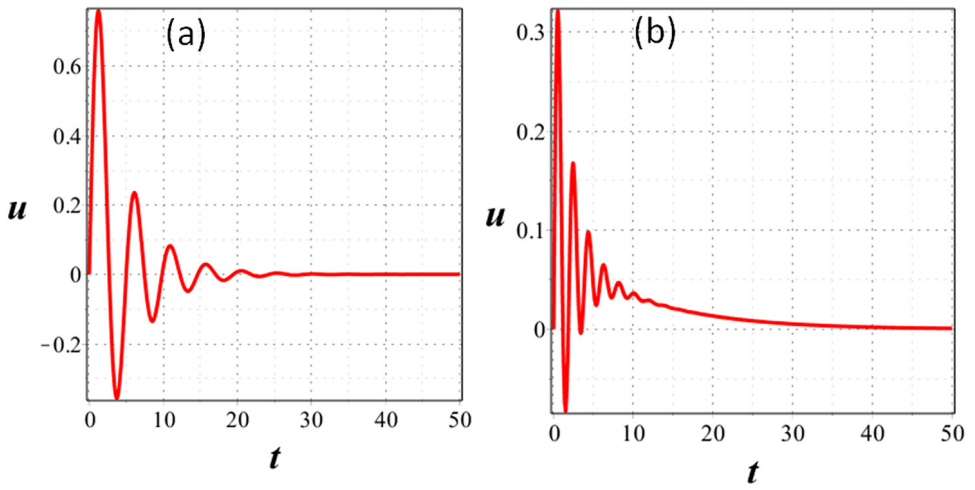

Fig. 3. Example of DT1 and DT2 shows the displacement with time (a) DT1, $\gamma > \beta$, (b) DT2, $\gamma < \beta$.

It should be noted that if $c \to \infty$, the SLS model (Fig. 2) behaves as two parallel spring–mass system with spring constants k and k_n. Hence the SLS system behaves as an undamped oscillator with two parallel spring systems, the natural frequency for which is given by,

$$n_1 = \frac{1}{2\pi}\sqrt{\frac{k+k_n}{m}}. \tag{25}$$

If $c \to 0$ SLS behave as a single spring–mass system with spring constant k. The undamped natural frequency in this system is given by

$$n_2 = \frac{1}{2\pi}\sqrt{\frac{k}{m}}. \tag{26}$$

Consider the case $k = k_n$ from Eqs. (25) and (26). In this case, the natural frequency relation is given by

$$n_1 = \sqrt{2}n_2. \tag{27}$$

To investigate the influence of the spring constant ratio ($R = k_n/k$) and the relaxation time on the solution, a parametric study is performed. For default values we set $\omega = 1$ for different values of R and τ. For c_1, c_2, c_3 in Eq. (24) assuming the following initial conditions:

$$u(0) = 0, \dot{u}(0) = v_o, \ddot{u}(0) = 0. \tag{28}$$

This gives

$$c_1 = \frac{2v_0\beta}{\alpha^2+\beta^2-2\beta\gamma+\gamma^2}, \tag{29}$$

$$c_2 = \frac{v_0\left(\alpha^2-\beta^2+\gamma^2\right)}{\left(\alpha^2+\beta^2-2\beta\gamma+\gamma^2\right)\alpha}, \tag{30}$$

$$c_3 = \frac{-2v_0\beta}{\alpha^2+\beta^2-2\beta\gamma+\gamma^2}, \tag{31}$$

where α, β, γ are taken from Eq. (18) to Eq. (23). Substituting c_1, c_2, c_3 into Eq. (24), gives the displacement (u) variation with time (t) for different values of R and τ.

Fig. 4(a) shows the variation of the displacement (u) with time (t) at $\tau = 1$ for $R = 0.1, 1, 10$. The vibrations are seen to be damped out rapidly as R increases from $R = 0.1, 1$ to 10. This behaviour is expected since as R increases, this results in an increase in k_n (assuming k is fixed), which decreases the motion velocity hence results in faster damping. Fig. 4(b) displays the displacement plot with time at $R = 1$ for $\tau = 0.1, 1, 10$. It shows the time to decay for damped vibration is non monotonic with τ. The time to decay at both $\tau = 10$ and 0.1 is less than the time to decay for $\tau = 1$. This behaviour is due to the SLS model, where for $\tau \to \infty$ and $\tau \to 0$ the system behaves as an undamped system.

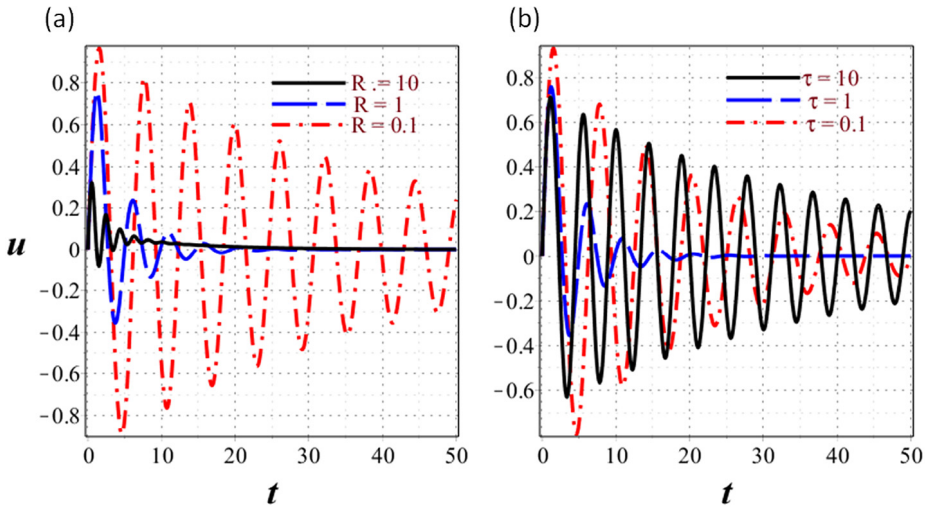

Fig. 4. Displacement versus time for different cases for (a) R = [10, 1, 0.1] at $\tau = 1$, (b) $\tau = [10, 1, 0.1]$ at $R = 1$.

3.2. Forced vibration

We consider the case of forced vibration of the form $F_{ext} = F_0 \cos(\Omega t)$ in this section. The equation of motion is then given by

$$\frac{mc}{k_n}\frac{d^3u}{dt^3} + m\frac{d^2u}{dt^2} + c\left(1 + \frac{k}{k_n}\right)\frac{du}{dt} + ku = F_0\cos(\Omega t) - \frac{c}{k_n}F_0\Omega\sin(\Omega t). \tag{32}$$

This equation can then be expressed in the form

$$\tau\frac{d^3u}{dt^3} + \frac{d^2u}{dt^2} + \tau\omega^2(1+R)\frac{du}{dt} + \omega^2 u = f_1\cos(\Omega t) - f_2\sin(\Omega t), \tag{33}$$

where f_1 and f_2 is given by,

$$\begin{aligned} f_1 &= \frac{F_0\omega^2}{k} \\ f_2 &= \frac{\tau F_0\Omega\omega^2}{k}. \end{aligned} \tag{34}$$

The solution of Eq. (33) consists of homogeneous and particular solutions. As homogeneous part decays, only the particular solution contributes to the steady solution. The particular solution is given by

$$u_p = a\cos(\Omega t) + b\sin(\Omega t), \tag{35}$$

where a and b are given by,

$$a = -\frac{-\Omega f_2\omega^2\tau(R+1) + \Omega^3 f_2\tau + f_1\left(\Omega^2 - \omega^2\right)}{D_r}, \tag{36}$$

$$b = -\frac{-\Omega f_1\omega^2\tau(R+1) + \Omega^3 f_1\tau + f_2\left(\omega^2 - \Omega^2\right)}{D_r}. \tag{37}$$

Here,

$$D_r = \Omega^2\omega^2\tau^2 R\left(\omega^2 R - 2\Omega^2 + 2\omega^2\right) + \left(\Omega^2\tau^2 + 1\right)\left(\Omega^2 - \omega^2\right)^2. \tag{38}$$

The amplitude of the vibration $A = \sqrt{a^2 + b^2}$ is given by

$$A = \frac{F_0}{k}\sqrt{\frac{1 + \omega^2\tau^2 r^2}{(1-r^2)^2 + \tau^2\omega^2 r^2\left((r^2-1)^2 + R^2 + 2R - 2Rr^2\right)}}, \tag{39}$$

where r is ratio of forcing frequency (Ω) to natural frequency (ω), i.e. $r = \Omega/\omega$. It is clear from Eq. (39), that the amplitude depends on the parameters r, R, τ, ω and F_0.

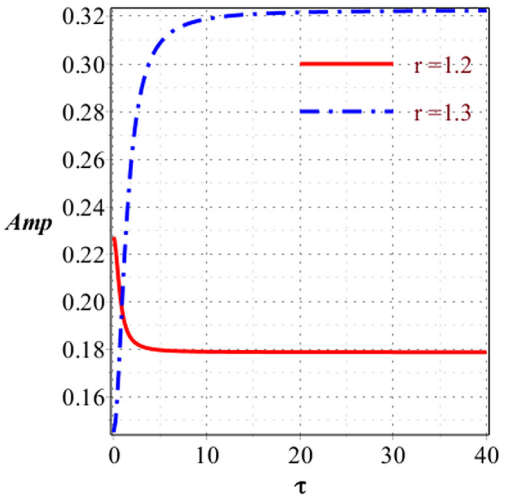

Fig. 5. Amplitude variation with τ at $R = 1$ for $r = 1.2$, 1.3 ($r_{cr} = \sqrt{1.5} = 1.22$).

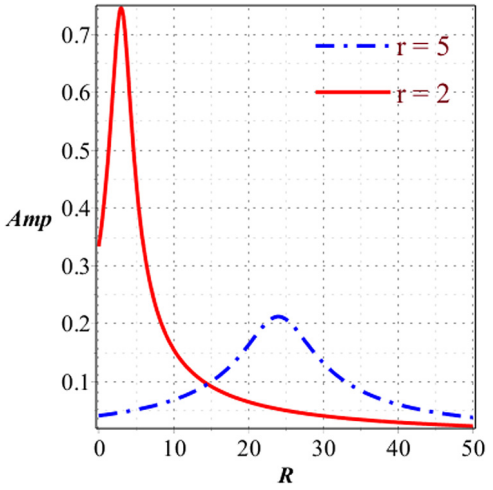

Fig. 6. Amplitude variation with R for $r = 5$ ($R_{cr} = 24$) and $r = 2$ ($R_{cr} = 3$).

If $R \to 1$, i.e. if $k = k_n$, Eq. (39) reduces to:

$$A = \frac{F_0}{k}\sqrt{\frac{1+\omega^2\tau^2r^2}{(1-r^2)^2+\tau^2\omega^2r^2((r^2-1)^2+3-2r^2)}}. \tag{40}$$

It should be noted that if $\tau \to 0$, only the spring with spring constant k is active, and the amplitude of the vibration is given by

$$A = \frac{F_0}{k|1-r^2|}, \tag{41}$$

whereas if $\tau \to \infty$, both the spring k and k_n are active and the amplitude of vibration is given by

$$A = \frac{F_0}{k|2-r^2|}. \tag{42}$$

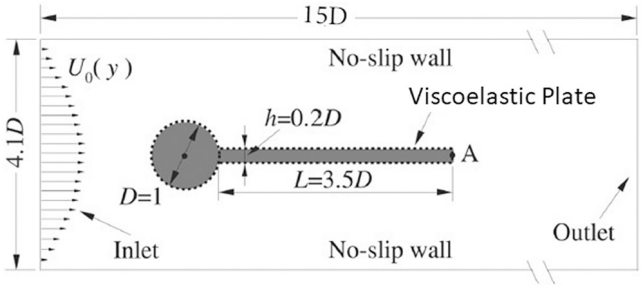

Fig. 7. Schematic of the flow domain with details of the boundary conditions. This FSI benchmark was proposed by Turek and Hron (2006) and extended to account for viscoelasticity of the plate in the present work.

3.2.1. Effect of τ on amplitude

It can be shown (see Appendix B) that the amplitude decreases for $r < r_{cr}$ and increases for $r > r_{cr}$. The critical value of r is given by

$$r_{cr} = \sqrt{\frac{R+2}{2}}. \tag{43}$$

The amplitude (A) decreases for $r < r_{cr}$ and increases for $r > r_{cr}$ asymptotically with τ, and for $\tau \to \infty$ achieves a constant state value, given by,

$$A = \frac{F_0}{k|1+R-r^2|}. \tag{44}$$

It is evident from Eq. (44) that the system is at resonance when $1+R = r^2$. The amplitude decays to zero for $1+R \gg r^2$, else it would attain a constant value of $F_0/(k|1+R-r^2|)$.

For $R = 1$, the amplitude is given by

$$A = \frac{F_0}{k}\sqrt{\frac{1+\omega^2\tau^2r^2}{(1-r^2)^2+\tau^2\omega^2r^2(r^2-2)^2}}. \tag{45}$$

For $R = 1$, from Eq. (43) $r_{cr} = \sqrt{1.5}$. Fig. 5 shows an example of the variation of amplitude with τ for parametric constants $\omega = 1, R = 1, k = 10$. As calculated, $r_{cr} = 1.22$ for $R = 1$, hence amplitude decreases with τ for $r = 1.2 < r_{cr}$, whereas the amplitude increases with τ for $r = 1.3 > r_{cr}$. For $r = r_{cr} = 1.22$, the amplitude is given by $2F_0/k$.

3.2.2. Effect of R on amplitude

The variation of amplitude with R is a non-monotonic function of R, as derived in Appendix C which shows that the amplitude increases with R up to R_{cr} and decreases beyond R_{cr} where

$$R_{cr} = r^2 - 1. \tag{46}$$

An example is shown in Fig. 6 for which $F = 10, \omega = 1, k = 10$, which shows the variation of amplitude with R for two values of $r = 2$ and 5. Amplitude increases for $R < R_{cr}$ beyond which it decreases.

4. Results and discussion

4.1. Computational domain and boundary conditions

The problem considered in the present study consists of a two-dimensional laminar channel flow past a viscoelastic plate attached to the lee side of a circular cylinder (Fig. 7). The flow configuration is similar to that investigated by Turek and Hron (2006). The fluid is considered to be incompressible and Newtonian. The boundary conditions are shown in Fig. 7 and are described as follows: At the inlet, a parabolic velocity profile with a mean velocity $U_m = 1$ is applied, and no-slip boundary conditions are applied to the channel walls and immersed structure boundary. Zero Neumann boundary condition is applied to the flow velocity at the right boundary. The following values are considered for the simulation: $U_m = 1, D = 1, Re = 100, \rho_s = 10, E_{eq} = 1.4 \times 10^3$. The mean velocity U_m and the cylinder diameter D are used as velocity and length reference scales, respectively to define the Reynolds number, $Re = U_mD/\nu$, where ν is the kinematic viscosity of the fluid. The plate consists of viscoelastic material under a plane strain condition with the assumption of small strain theory. The relaxation time for the shear and bulk stresses are assumed to be the same.

The computational domain size in the current simulation is $0 \le x \le 15D$ and $0 \le y \le 4.1D$, discretized using a 385×193 cell non-uniform Cartesian grid with uniform spacing near the cylinder and the plate with $\Delta x_{min} = \Delta y_{min} =$

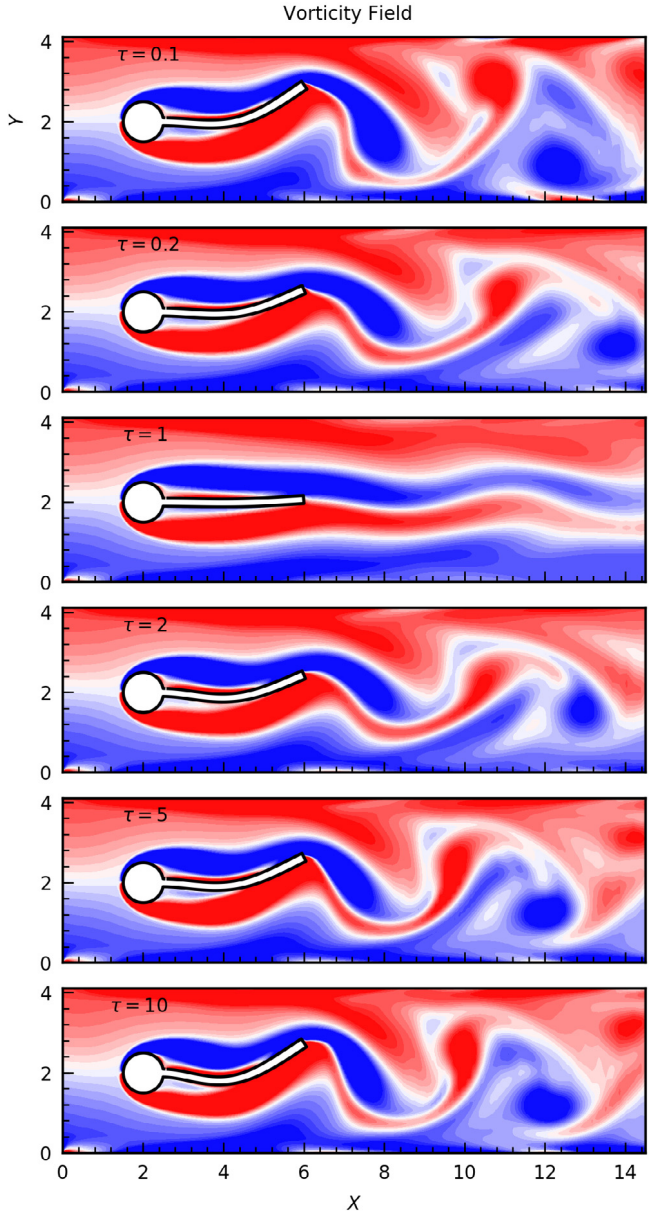

Fig. 8. Vorticity field for different cases of $\tau = [0.1, 0.2, 1, 2, 5, 10]$ for $R = 1$ at the instance of the plate maximum displacement. The contour map range is $[-2, 2]$.

0.019. The time step for the flow as well as the structure solver is $\Delta t = 0.01$. The flow and structure grid sizes, as well as the time step, are based on a resolution study, reported in our previous paper (Kundu et al., 2017). The cylinder and plate are discretized with a three-node triangular mesh with 5792 triangular elements and 3089 nodes. In the following sub-sections, we present results of simulations, carried out for different values of $\tau(= \eta/E_{neq})$ and $R(= E_{neq}/E_{eq})$. Typical computed vorticity fields for different cases of τ at $R = 1$ are shown in Fig. 8.

4.2. Response of the viscoelastic plate at $\tau \to 0$ and $\tau \to \infty$

Here, the response of the linear viscoelastic plate is compared with a linear elastic plate for the limiting cases of $\tau \to 0$ ($\tau = 1 \times 10^{-16}$ taken in the FSI solver) and $\tau \to \infty$ ($\tau = 1 \times 10^{16}$) to show that the viscoelastic plate behaves as elastic plate at the extreme cases of τ. For the elastic material $E = 1.4 \times 10^3$ and $E = 2.8 \times 10^3$ are examined, whereas for the viscoelastic material $E_{neq} = E_{eq} = 1.4 \times 10^3$. Fig. 9 displays the time evolution of the y displacements of the plate tip for (a) $E = 1.4 \times 10^3$ and (b) $E = 2.8 \times 10^3$. Here, the flow induces a wave-like deformation in the plate, and the

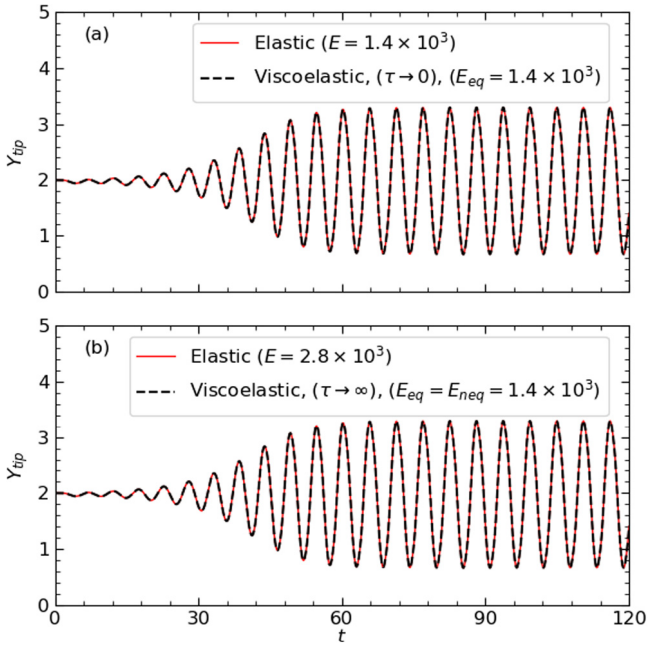

Fig. 9. Time-varying tip displacement for elastic and viscoelastic plates (a) $\tau \to 0$ (b) $\tau \to \infty$.

plate attains self-sustained periodic oscillations with a constant amplitude after a short time. It clearly shows that the viscoelastic plate behaves as elastic plate for (a) $\tau \to 0$ and (b) $\tau \to \infty$. It can be seen that the amplitude is smaller for the case (b) $\tau \to \infty$. This occurs due to large bending stiffness at $\tau \to \infty$. Note that equivalent Young's modulus is $E_{equivalent} = E_{eq}$ for $\tau \to 0$, whereas $E_{equivalent} = E_{eq} + E_{neq}$ for $\tau \to \infty$.

4.3. Response of the viscoelastic plate for intermediate values of τ

In order to identify the effects of the structural damping, τ, and the ratio of Young's moduli of the splitter plate, R, on the vibration of the plate, a series of simulations was undertaken for the flow past a cylinder with a splitter viscoelastic plate by varying τ and R. The boundary conditions are the same as those described in Section 2, and are shown in Fig. 7. The tip displacement, time to achieve dynamic steady state and lift have been determined for different R and τ. In particular, the time varying tip displacement of the plate with $R = 0.1, 0.5, 1, 2, 5, 10$ for $\tau = 0.1, 0.2, 1, 2, 5, 10$ has been studied. For R below 0.1, the displacement is large as the bending stiffness of the plate decreases. Hence, $R < 0.1$ is not considered further because of the small strain assumption in the model.

4.3.1. Effect of τ and R on the amplitude of the tip

The amplitude of the tip displacement ($A_{Y,tip}$) of the plate with τ for $R = 0.1, 0.5, 1, 2$ is shown in Fig. 10(a). It shows that for $R = 0.1, 0.5, 1$ and 2, $A_{Y,tip}$ decreases with τ near $\tau = 1$, beyond which $A_{Y,tip}$ again increases with τ asymptotically approaching a constant value. This effect is more prominent for $R = 1$, whereas for $R = 5$ and beyond, $A_{Y,tip}$ decreases with increasing τ. This behaviour is similar to that predicted by the mass–spring–dashpot (MSD) model discussed in Section 3.2, and is discussed as follows. Analytically, using the MSD model, Eq. (43) gives $r_{cr} = 1.1, 1.2$ and 1.4 for $R = 0.5, 1$ and 2, respectively. Tables 2–4 quantify the variation of $A_{Y,tip}$ with τ and r, corresponding to $R = 0.5, 1, 2$, respectively. In all Tables, f_{n,E_∞} is the natural frequency of the elastic plate with Young's modulus E_∞ and $f_{n,E_\infty+E_0}$ is the natural frequency of an elastic plate considering Young's modulus $E_\infty + E_0$. This initially surprising, non-monotonic behaviour can be explained by considering the MSD SLS model, which behaves as an undamped system in the limiting cases of τ. For intermediate values of τ, material damping exists which decreases the amplitude. Therefore, the amplitude is larger at very small and very large values of τ, whereas the amplitude is lower for the intermediate values. Further, the amplitude is larger at lower values of τ than higher values of τ because of the larger bending stiffness at $\tau \to \infty$. As explained above, the equivalent Young's modulus is $E_{equivalent} = E_{eq}$ for $\tau \to 0$, whereas $E_{equivalent} = E_{eq} + E_{neq}$ for $\tau \to \infty$.

The natural frequencies in first, second and third modes respectively (considering E_{eq} and using Eq. (47)) for the plate are $f_n = 0.03, 0.20$ and 0.55, respectively. The superimposed snapshots of the deformed plate at different instances for $R = 1$ and 2 for $\tau = 5$ are shown in Fig. 11(a) and (b) respectively. We have found through selecting different values of R and τ that the plate vibrates with the second mode, although the amplitude may vary. In this context Lee and You (2013) and Kundu et al. (2017) also observed that an elastic plate oscillates with a frequency close to the second mode

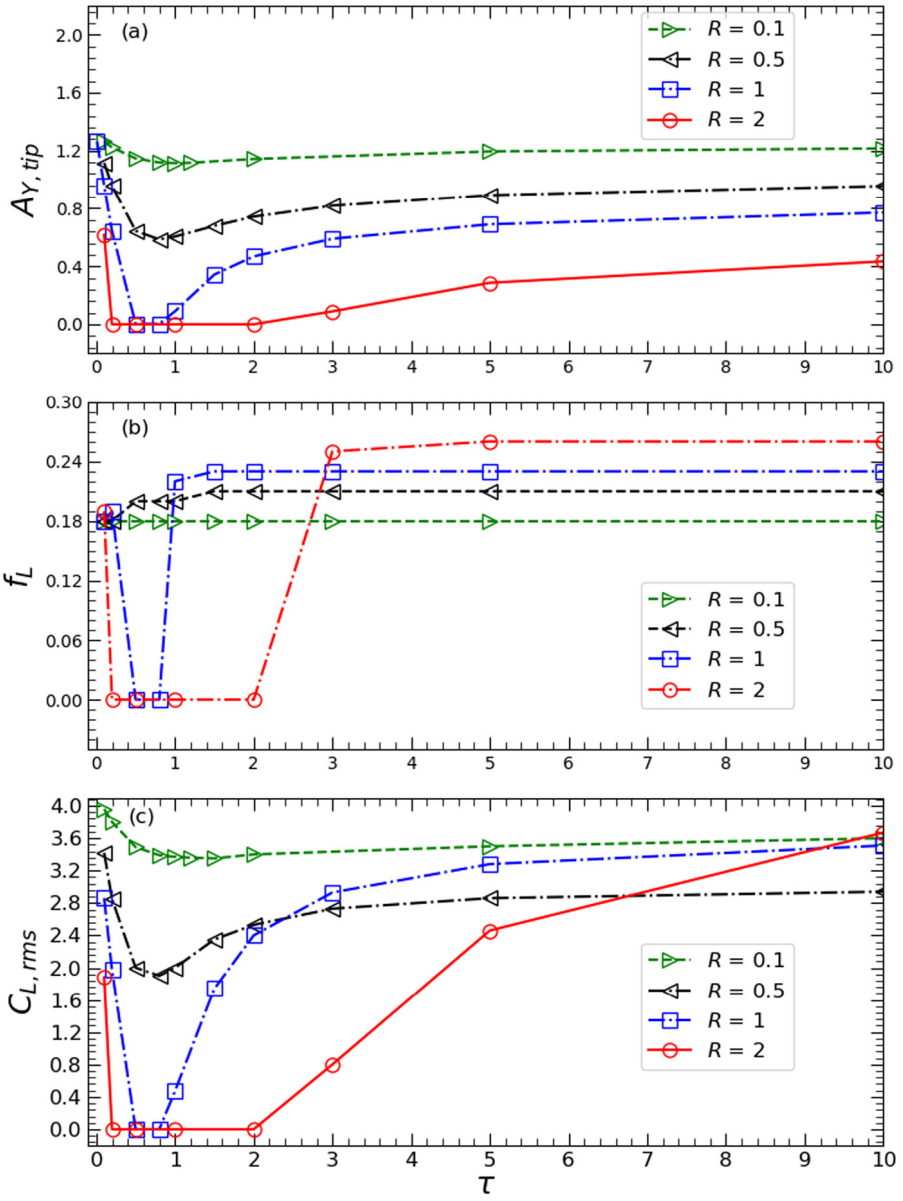

Fig. 10. Variation of (a) amplitude of viscoelastic plate tip ($A_{Y,tip}$), (b) frequency of lift coefficient (f_L), and (c) root mean square lift coefficient ($C_{L,rms}$) with τ for $R = [0.1, 0.5, 1, 2]$.

of natural frequency for $l = 3.5D$. We consider $f_n = 0.20$ case, based on which r is calculated. The non-dimensionalized forcing frequency (f) is obtained from the FFT of the lift coefficient (C_L) signal. This corresponds to the Strouhal number of vortex shedding or the frequency of periodic deflection. The forcing frequency is depicted in Fig. 10(b), which shows the variation of plate frequency (f) with τ. Similar behaviour is observed for the simple MSD model for sinusoidal forcing as the FSI response also shows a sinusoidal lift force, hence if $r < r_{cr}$, $A_{Y,tip}$ decreases with τ, while if $r > r_{cr}$, $A_{Y,tip}$ increases with τ. These behaviours are shown in Fig. 10. It is also observed from Fig. 10(c), which plots root mean square value of lift coefficient ($C_{L,rms}$) as a function of τ. This shows that the magnitude of $C_{L,rms}$ reduces as τ increases, and again $C_{L,rms}$ increases by further increasing τ. We plot vorticity field for different cases of τ at $R = 1$ in Fig. 8 and note that vortices shed from the tip of the plate in all cases expect in the case of $\tau = 1$, implying a zero value of $C_{L,rms}$ in this case, as plotted in Fig. 10(c).

It is also observed from Tables 2–4, that as R increases the size of the non-vibrating region increases. This is because of the competing effects of τ and R. This can be explained of the plate using the MSD model. If $\tau = c/k_n$ is constant, and assuming c and k_n are constant, as $R = k_n/k$ increases k decreases. It can be observed that if $k = 0$, the MSD model (Fig. 2)

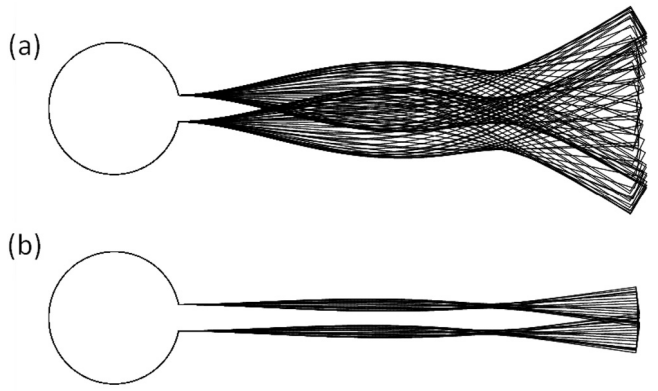

Fig. 11. Vibration modes of the FSI system at $\tau = 5$ for (a) $R = 1$, (b) $R = 2$.

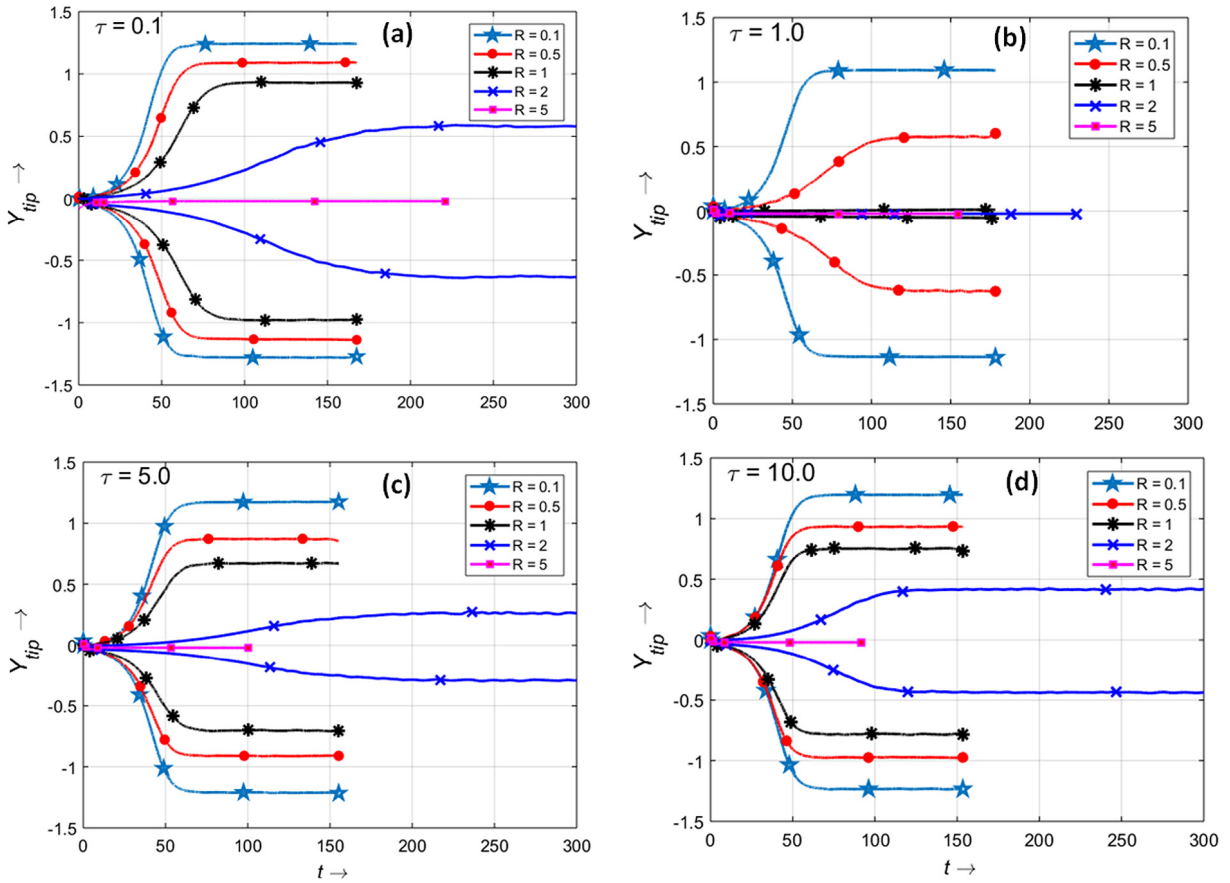

Fig. 12. Time to achieve dynamic steady state shown as the envelope of the time-varying tip displacements of a viscoelastic plate for $R = 0.1, 0.5, 1, 2, 5$, for (a) $\tau = 0.1$, (b) $\tau = 1$, (c) $\tau = 5$, and (d) $\tau = 10$. (For interpretation of the references to colour in this figure legend, the reader is referred to the web version of this article.)

represents a spring–dashpot in series, whereas for $k \to \infty$ there is no vibration. Also, if k is constant, on increasing R, k_n increases. For $k_n = 0$, the MSD model behave as the vibration of a single spring (no dashpot) of spring constant k, while for $k_n \to \infty$ the MSD model behaves as a spring (spring constant k) and dashpot (c) in parallel, so that the vibration decays with increasing c.

4.3.2. Time to achieve dynamic steady-state

The time to achieve a dynamic steady state (t_{ss}) varies with τ and R. The initial conditions of all the simulations are same. Fig. 12 displays the envelope of time varying Y_{tip} for $R = 0.1, 0.5, 1, 2, 3, 5$ corresponding to each of

Table 1
Nomenclature used in the present paper.

Symbol	Definition
D^*	Diameter of cylinder [m]
E_{neq}	Non-equilibrium Young's modulus of the viscoelastic plate ($E^*_{neq}/\rho^*_f U^{*2}_m$)
E_{eq}	Equilibrium Young's modulus of the viscoelastic plate ($E^*_{eq}/\rho^*_f U^{*2}_m$)
η	Structural damping of the viscoelastic plate ($\eta^*/\rho^*_f U^*_m D$)
R	Ratio of the non-equilibrium to equilibrium Young's modulus (E_{neq}/E_{eq})
τ	Ratio of structural damping to non-equilibrium Young's modulus (η/E_{neq})
U_m	Mean velocity at the left boundary of channel [m/s]
Y_{tip}	Cross-stream displacement of tip of the plate (Y^*_{tip}/D^*)
ρ_s	Ratio of density of the structure to the fluid (ρ^*_s/ρ^*_f)
r	Ratio of forcing frequency to natural frequency of structure (Ω/ω)
$A_{Y,tip}$	Amplitude of vibration of tip of plate ($A^*_{Y,tip}/D^*$)
Superscripts	
$*$	Dimensional quantity
Acronyms	
FSI	Fluid–structure interaction
IB	Immersed boundary
KV	Kelvin–Voigt
MSD	Mass–spring–dashpot
SLS	Standard linear solid

Table 2
Frequency of fluid force (f) for $R = 0.5$ (MSD, $r_{cr} = 1.1$) with τ and $r = f/f_n$.

$f_{n,E_\infty} = 0.20$, $f_{n,E_\infty+E_0} = 0.24$

τ	f	r $= f/f_n$	$A_{Y,tip}$	Remarks
0.1	0.18	0.9	1.116	$r < r_{cr}$
0.2	0.18	0.9	0.956	$r < r_{cr}$
0.5	0.20	1	0.644	$r < r_{cr}$
0.8	0.20	1	0.585	$r < r_{cr}$
1	0.20	1	0.605	$r < r_{cr}$
1.5	0.21	1.1	0.679	$r \geq r_{cr}$
2	0.21	1.1	0.743	$r \geq r_{cr}$
3	0.21	1.1	0.819	$r \geq r_{cr}$
5	0.21	1.1	0.892	$r \geq r_{cr}$
10	0.21	1.1	0.955	$r \geq r_{cr}$

Table 3
Frequency of fluid force (f) for $R = 1$ (MSD, $r_{cr} = 1.2$) with τ and $r = f/f_n$.

$f_{n,E_\infty} = 0.20$, $f_{n,E_\infty+E_0} = 0.28$

τ	f	r $= f/f_n$	$A_{Y,tip}$	Remarks
0.1	0.18	0.9	1.263	$r < r_{cr}$
0.2	0.19	0.95	0.956	$r < r_{cr}$
0.5	0		0	No vibration
0.8	0		0	No vibration
1	0.22	1.1	0.09	$r < r_{cr}$
1.5	0.23	1.2	0.343	$r \geq r_{cr}$
2	0.23	1.2	0.468	$r \geq r_{cr}$
3	0.23	1.2	0.59	$r \geq r_{cr}$
5	0.23	1.2	0.69	$r \geq r_{cr}$
10	0.23	1.2	0.771	$r \geq r_{cr}$

$\tau = 0.1, 1, 5, 10$. In Fig. 12, the envelope terminates at different times corresponding to the changing times to reach a steady state. Fig. 12 shows that for $R = 5$ there is no vibration and this continues for $R > 5$. We found for $\tau = 0.1$, the time to achieve steady state increases as R increases from $0.1, 0.5, 1, 2$ (Fig. 12(a)). A similar trend is observed for $\tau = 1, 5, 10$ as well. It has been found that for $R = 0.5, 1, 2$, t_{ss} ($R = 0.5$ red, $R = 1$ blue and $R = 2$ blue) increases for $\tau = 0.1, 1$, whereas t_{ss} again decreases for $\tau = 5$ and 10. This non-monotonic variation of t_{ss} is due to the SLS model, where for very low and high values of τ system behaves as an undamped system. It has been explained by the free

Table 4
Frequency of fluid force (f) for $R = 2$ (MSD, $r_{cr} = 1.4$) with τ and $r = f/f_n$.
$f_{n,E_\infty} = 0.20$, $f_{n,E_\infty+E_0} = 0.34$

τ	f	r $= f/f_n$	$A_{Y,tip}$	Remarks
0.1	0.19	0.95	0.616	$r < r_{cr}$
0.2	0		0	No vibration
0.5	0		0	No vibration
0.8	0		0	No vibration
1	0		0	No vibration
1.5	0		0	No vibration
2	0		0	No vibration
3	0.25	1.3	0.089	$r \approx r_{cr}$
5	0.26	1.3	0.286	$r \approx r_{cr}$
10	0.26	1.3	0.434	$r \approx r_{cr}$

Table A.1
Simulation results for different cases considered for free vibration of a viscoelastic cantilevered beam with structure density ratio ($\rho = 10$) and plate length (L=3.5). Young's Modulus takes the values 1400 and 1000. The Poisson ratio and plate thickness are 0.4 and 0.2, respectively, in all cases.

Cases	τ	$E_{neq} = E_{eq}$	n_1	n_2	n_3	Remarks
1	0	1400	0.034	0.2124	0.576	
2	∞	1400	0.048	0.300	0.8154	$n_{\tau\to\infty} = \sqrt{2}n_{\tau\to 0}$
3	0	1000	0.029	0.178	0.4883	
4	∞	1000	0.041	0.253	0.688	$n_{\tau\to\infty} = \sqrt{2}n_{\tau\to 0}$

vibration of the MSD model (Section 3.1). The MSD model illustrates that for each R as τ increases, t_{ss} increases for lower values of τ, whereas t_{ss} again decreases for higher values of τ. Therefore, the non-monotonic variation of t_{ss} obtained by the FSI solver is consistent with the homogeneous solution of the MSD model.

5. Conclusions

Extending previous studies based on elastic materials, the dynamics of a *viscoelastic* plate attached to a rigid cylinder and immersed in an incompressible flow has been studied numerically in this paper. While the study was undertaken for a low Reynolds number of $Re = 100$, it seems likely that, at least to some extent, the main findings should be transferable to higher Reynolds number cases. The standard linear solid (SLS) model is used to model the viscoelasticity of the material. The simulations have been carried out using an in-house code FSI solver combining a sharp-interface immersed boundary method flow solver and an open-source finite-element based structural solver. It is observed that the vibration amplitude of the plate is governed by the damping coefficient of the plate and the ratio of non-equilibrium to equilibrium modulus (R). For a fixed value of R in the range $0 < R < 2$, the amplitude of vibration is found to be a non-monotonic function of the damping. For $R > 2$, the vibration is suppressed altogether. This non-monotonic behaviour is explained by considering the vibration of a lumped spring–mass–damper SLS model. Such a model was developed and analysed as part of this research and is presented in this paper. Importantly, the present results indicate that it may be possible to tune the behaviour of a structural system by actively modifying the damping. This approach could be potentially exploited for applications that require control of flow-induced vibrations. For example, in energy harvesting applications, it could allow tuning of the damping to generate large amplitude oscillations to maximize power output, while in other cases where FIV is detrimental, oscillations could be suppressed altogether.

Acknowledgement

R.B. gratefully acknowledges financial support from the Naval Research Board (NRB), India through grant NRB-403/-HYD/17-18.

Appendix A. Free vibration of viscoelastic plate

Basic structure validation of SLS is done in Tahoe (2001) for free vibration of a cantilevered plate. We consider a plate of length $3.5D$ and thickness $0.2D$ similar to the FSI system. The natural frequency is calculated for an undamped system for extreme cases. First, when viscosity is very high, i.e. $\tau \to \infty$ and second, when viscosity is very low, i.e. $\tau \to 0$. The natural frequencies (f_i) of the plate for the first three modes using simulation results are shown in Table A.1. Using the Euler–Bernoulli beam model, the natural frequency (f_i) of the vibration of a cantilever beam is given by,

$$f_i = \frac{k_i^2}{2\pi}\sqrt{\frac{EI}{\rho AL^4}}. \tag{47}$$

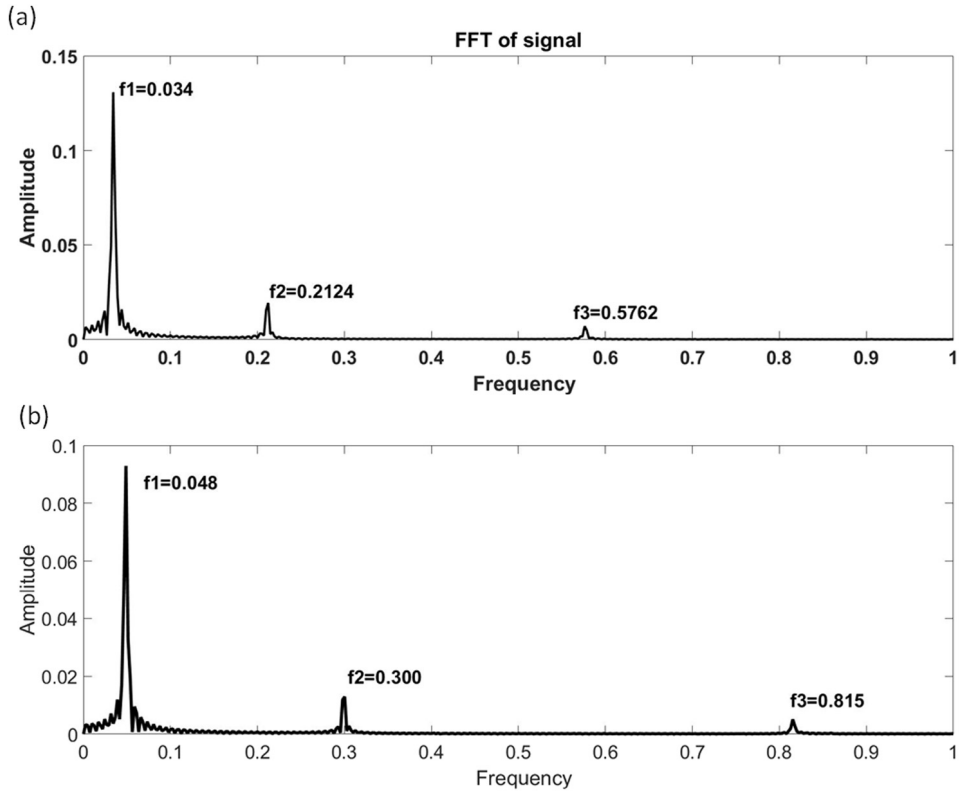

Fig. A.1. Power spectra of Y_{tip} displacement of viscoelastic plate for $E_{neq} = E_{eq} = 1400$ (a) $\tau \to 0$, (b) $\tau \to \infty$.

where EI is the flexural rigidity of the beam, $i = 1, 2, 3$ represents frequency modes of the plate, and k is the respective constant for the modes. Here, ρ, A and L are density, cross-sectional area and length of the plate, respectively. The values of k are 1.875, 4.694 and 7.855 for the first, second and third modes for the natural frequencies, respectively.

Table A.1 shows the first (n_1), second (n_2) and third (n_3) mode frequencies for $E_{neq} = E_{eq} = 1400$ and $E_{neq} = E_{eq} = 1000$ at $\tau \to \infty$ and $\tau \to 0$. It evident that for all modes $\tau \to \infty$ is $\sqrt{2}$ times the natural frequency for $\tau \to 0$. This behaviour occurs because for $\tau \to 0$ SLS behaves as single spring–mass system with spring constant k, whereas for $\tau \to \infty$ SLS behaves as two parallel spring–mass systems with spring constants k, k_n. Fig. A.1 shows the power spectra of Y_{tip} with time for a non dimensional Young's Modulus of 1400 for two extreme cases Fig. A.1(a) $\tau \to 0$ and Fig. A.1(b) $\tau \to \infty$. The frequencies, n_i, obtained in the two cases are close to the respective frequencies, f_i, obtained using Eq. (47) (within maximum error of 10%), and thereby validating the present structural solver.

Appendix B. Effect of τ on the amplitude of forced vibration

The amplitude of sinusoidal force vibration is given by Eq. (39):

$$A = \frac{F_0}{k}\sqrt{\frac{1+\omega^2\tau^2 r^2}{(1-r^2)^2+\tau^2\omega^2 r^2((r^2-1)^2+R^2+2R-2Rr^2)}}. \tag{48}$$

To know the effect of amplitude on τ, Eq. (48) is differentiated with respect to τ, assuming other variables remain constant.

$$\frac{dA}{d\tau} = 0. \tag{49}$$

$$-\frac{\omega^2 r^2 \tau F_0^2 R(-2r^2+R+2)}{\sqrt{Tr}} = 0. \tag{50}$$

where

$$Tr = F_0^2(\omega^2 r^2\tau^2+1)(\omega^2 r^6\tau^2 - 2R\omega^2 r^4\tau^2 + R^2\omega^2 r^2\tau^2 - 2\omega^2 r^4\tau^2$$

$$+2R\omega^2r^2\tau^2+\omega^2r^2\tau^2+r^4-2r^2+1)k^2. \tag{51}$$

Since ω, r, τ and F_0 are positive, then r_{cr} is given by

$$r_{cr}=\sqrt{\frac{R+2}{2}}. \tag{52}$$

Clearly from Eq. (50), A decreases with τ if $r_{cr}<\sqrt{(R+2)/2}$.

It should be noted that amplitude is defined for positive values of the expression inside the square root, i.e. A is defined for the following inequality

$$(1-r^2)^2+\tau^2\omega^2r^2((r^2-1)^2+R^2+2R-2Rr^2)>0. \tag{53}$$

For $R=1$, the amplitude is given by

$$A=\frac{F_0}{k}\sqrt{\frac{1+\omega^2\tau^2r^2}{(1-r^2)^2+\tau^2\omega^2r^2(r^2-2)^2}}. \tag{54}$$

Appendix C. Effect of R on the amplitude of forced vibration

To know the effect of amplitude on R, Eq. (48) is differentiated with respect to R assuming other variables remain constant.

$$\frac{dA}{dR}=0. \tag{55}$$

$$-\frac{(\omega^2r^2\tau^2+1)F_0^2r^2\omega^2\tau^2(-r^2+R+1)}{\sqrt{Tr}}=0. \tag{56}$$

where Tr is same term as in Eq. (51). Clearly r_{cr} in terms of R, and assuming ω, τ, F_0 are fixed, is given by

$$R_{cr}=r^2-1. \tag{57}$$

The amplitude is non-monotonic function of R. It is evident from Eq. (56) that the amplitude increases with R for $R<R_{cr}$, while it decreases for $R>R_{cr}$.

Appendix D. Real roots of the characteristic equation

Let r_1, r_2, r_3 be the three real roots of the characteristic equation

$$\tau r^3+r^2+\tau\omega^2(1+R)r+\omega^2=0. \tag{58}$$

For the roots of a cubic equation

$$\begin{aligned} r_1+r_2+r_3&=-\frac{1}{\tau},\\ r_1r_2+r_2r_3+r_1r_3&=\frac{\tau\omega^2(1+R)}{\tau},\\ r_1r_2r_3&=-\frac{\omega^2}{\tau}. \end{aligned} \tag{59}$$

As ω, τ and $\tau\omega^2(1+R)$ are positive, therefore Eq. (59) holds only when r_1, r_2, r_3 are all negative.

References

Bailoor, S., Annangi, A., Seo, J.H., Bhardwaj, R., 2017. Fluid–structure interaction solver for compressible flows with applications to blast loading on thin elastic structures. Appl. Math. Model. 52, 470–492.

Bhardwaj, R., Mittal, R., 2012. Benchmarking a coupled immersed-boundary-finite-element solver for large-scale flow-induced deformation. AIAA J. 50 (7), 1638–1642.

Bhardwaj, R., Sharma, A., 2017. In: Chhabra, R.P. (Ed.), CRC Handbook of Thermal Engineering: Chapter 5.6: Immersed boundary method for Fluid-Structure Interaction Simulations. CRC Press (Taylor Francis).

Chen, M., Jia, L.-B., Chen, X.-P., Yin, X.-Z., 2014. Flutter analysis of a flag of fractional viscoelastic material. J. Sound Vib. 333 (26), 7183–7197.

Christensen, R., 2012. Theory of Viscoelasticity: An Introduction. Elsevier.

Connell, B.S., Yue, D.K., 2007. Flapping dynamics of a flag in a uniform stream. J. Fluid Mech. 581, 33–67.

De Haan, Y., Sluimers, G., 2001. Standard linear solid model for dynamic and time dependent behaviour of building materials. HERON 46 (1).

Eloy, C., Souilliez, C., Schouveiler, L., 2007. Flutter of a rectangular plate. J. Fluids Struct. 23 (6), 904–919.

Esmailzadeh, E., Jalali, M., 1999. Nonlinear oscillations of viscoelastic rectangular plates. Nonlinear Dynam. 18 (4), 311–319.

Fadlun, E., Verzicco, R., Orlandi, P., Mohd-Yusof, J., 2000. Combined immersed-boundary finite-difference methods for three-dimensional complex flow simulations. J. Comput. Phys. 161 (1), 35–60.
Findley, W.N., Davis, F.A., 2013. Creep and relaxation of nonlinear viscoelastic materials. Courier Corporation.
Furquan, M., Mittal, S., 2015. Flow past two square cylinders with flexible splitter plates. Comput. Mech. 55 (6), 1155–1166.
Huang, T.C., Huang, C., 1971. Free vibrations of viscoelastic Timoshenko beams. J. Appl. Mech. 38 (2), 515–521.
Ilyasov, M.H., Ilyasova, N.M., 2006. Flutter of viscoelastic strips. Mech. Time-Depend. Materials 10 (3), 201–213.
Keramat, A., Tijsseling, A., Hou, Q., Ahmadi, A., 2012. Fluid–structure interaction with pipe-wall viscoelasticity during water hammer. J. Fluids Struct. 28, 434–455.
Kiiko, I., 1996. Flutter of a viscoelastic plate. J. Appl. Math. Mech. 60 (1), 167–170.
Kundu, A., Soti, A.K., Bhardwaj, R., Thompson, M.C., 2017. The response of an elastic splitter plate attached to a cylinder to laminar pulsatile flow. J. Fluids Struct. 68, 423–443.
Lee, J., You, D., 2013. Study of vortex-shedding-induced vibration of a flexible splitter plate behind a cylinder. Phys. Fluids 25 (11), 110811.
Matyash, V., 1971. Flutter of a viscoelastic plate. Polymer Mech. 7 (6), 957–961.
Miao, S., Hendrickson, K., Liu, Y., 2017. Computation of three-dimensional multiphase flow dynamics by fully-coupled immersed flow (fcif) solver. J. Comput. Phys. 350, 97–116.
Mittal, R., 2004. Computational modeling in biohydrodynamics: trends, challenges, and recent advances. IEEE J. Ocean. Eng. 29 (3), 595–604.
Mittal, R., Dong, H., Bozkurttas, M., Najjar, F., Vargas, A., von Loebbecke, A., 2008. A versatile sharp interface immersed boundary method for incompressible flows with complex boundaries. J. Comput. Phys. 227 (10), 4825–4852.
Mittal, R., Iaccarino, G., 2005. Immersed boundary methods. Annu. Rev. Fluid Mech. 37, 239–261.
Mittal, R., Seo, J.H., Vedula, V., Choi, Y.J., Liu, H., Huang, H.H., Jain, S., Younes, L., Abraham, T., George, R.T., 2016. Computational modeling of cardiac hemodynamics: current status and future outlook. J. Comput. Phys. 305, 1065–1082.
Mittal, R., Zheng, X., Bhardwaj, R., Seo, J.H., Xue, Q., Bielamowicz, S., 2011. Toward a simulation-based tool for the treatment of vocal fold paralysis. Front. Physiol. 2, 19.
Peskin, C.S., 1972. Flow patterns around heart valves: a numerical method. J. Comput. Phys. 10 (2), 252–271.
Rogosin, S., Mainardi, F., 2014. George william scott blair–the pioneer of factional calculus in rheology. arXiv preprint arXiv:1404.3295.
Seo, J.H., Mittal, R., 2011. A sharp-interface immersed boundary method with improved mass conservation and reduced spurious pressure oscillations. J. Comput. Phys. 230 (19), 7347–7363.
Shelley, M., Vandenberghe, N., Zhang, J., 2005. Heavy flags undergo spontaneous oscillations in flowing water. Phys. Rev. Lett. 94 (9), 094302.
Shukla, S., Govardhan, R., Arakeri, J., 2013. Dynamics of a flexible splitter plate in the wake of a circular cylinder. J. Fluids Struct. 41, 127–134.
Tahoe, 2001. Tahoe Is an Open Source C++ Finite Element Solver. Sandia National Labs, CA, http://sourceforge.net/projects/tahoe/.
Turek, S., Hron, J., 2006. Proposal For Numerical Benchmarking of Fluid-Structure Interaction Between an Elastic Object and Laminar Incompressible Flow. In: Lecture notes in computational science and engineering, 53, Springer, p. 371.
Udaykumar, H., Mittal, R., Rampunggoon, P., Khanna, A., 2001. A sharp interface Cartesian grid method for simulating flows with complex moving boundaries. J. Comput. Phys. 174 (1), 345–380.
Wang, Z., Wood, N.B., Xu, X.Y., 2015. A viscoelastic fluid–structure interaction model for carotid arteries under pulsatile flow. Int. J. Numer. Methods Biomed. Eng. 31 (5), e02709.